Conf

LA-UR 91-4041

LA-UR--91-4041

DE92 005056

Los Alamos National Laboratory is operated by the University of California for the United States Department of Energy under contract W-7405-ENG-36.

TITLE: PHYSICAL PROCESSES AND EFFECTS OF MAGMATISM IN THE YUCCA MOUNTAIN REGION

AUTHOR(S): Greg A. Valentine, EES-5
Bruce M. Crowe, EES-13
Frank V. Perry, University of New Mexico

SUBMITTED TO: International High Level Radioactive Waste Management Conference (Proceedings), April 1992.

DISCLAIMER

Los Alamos Los Alamos National Laboratory
Los Alamos, New Mexico 87545

FORM NO. 836 R4
ST. NO. 2629 5/81

PHYSICAL PROCESSES AND EFFECTS OF MAGMATISM IN THE YUCCA MOUNTAIN REGION

Greg A. Valentine, Geoanalysis Group EES-5, MS F665, Los Alamos National Laboratory, Los Alamos, NM 87545

Bruce M. Crowe, Nuclear Waste Management Group EES-13, MS J521, Los Alamos National Laboratory, Los Alamos, NM 87545

Frank V. Perry, Geology Department, University of New Mexico, Albuquerque, NM 87131

ABSTRACT

This paper describes initial studies related to the effects of volcanism on performance of the proposed Yucca Mountain radioactive waste repository, and to the general processes of magmatism in the Yucca Mountain region. Volcanism or igneous activity can affect the repository performance by ejection of waste onto the earth's surface (eruptive effects), or by subsurface effects of hydrothermal processes and altered hydrology if an intrusion occurs within the repository block. Initial, conservative calculations of the volume of waste that might be erupted during a small-volume basaltic eruption (such as those which have occurred in the Yucca Mountain region) indicate that regulatory limits might be exceeded. Current efforts to refine these calculations, based upon field studies at analog sites, are described. Studies of subsurface effects are just beginning, and are currently focussed on field studies of intrusion properties and contact metamorphism at deeply eroded analog sites. General processes of magmatism are important for providing a physical basis for predictions of future volcanic activity. Initial studies have focussed on modeling basaltic magma chambers in conjunction with petrographic and geochemical studies. An example of the thermal-fluid dynamic evolution of a small basaltic sill is described, based on numerical simulation. Quantification of eruption conditions can provide valuable information on the overall magmatic system. We are developing quantitative methods for mapping pyroclastic facies of small basaltic centers and, in combination with two-phase hydrodynamic simulation, using this information to estimate eruption conditions. Examples of such hydrodynamic simulations are presented, along with comparison to an historical eruption in Hawaii.

INTRODUCTION

This paper reports studies of three classes of issues related to magmatism at Yucca Mountain. The first of these is the consequence of small-volume basaltic eruptions penetrating the repository. Work related to this issue is focussed primarily on constraining the volume of waste that could be erupted onto the surface of Yucca Mountain (the accessible environment), and relies on data collected from analog volcanoes in the southwestern United States. The second class of issues is that of subsurface effects of magmatic activity within the repository block, regardless of whether such activity produces a surface eruption. A combination of analog studies at deeply eroded basaltic centers and modeling of hydrothermal/magmatic processes is being used to understand the means by which this subsurface activity may accelerate the release of waste to the accessible environment. The third class of issues relates to general physical mechanisms of magmatism in the Yucca Mountain region, including melt generation, storage, ascent, and eruption. The goal of this research is to tie regional and local geophysical, petrochemical, geochronological, and geological observations with physical processes in order to provide a mechanistic foundation for predictions of volcanic activity.

The risk (R) of volcanic activity at Yucca Mountain during the lifetime of the proposed repository has been defined as

$$R = \{E1 * E2 * E3\} \quad , \qquad (1)$$

where $E1$ is the probability of an event in the Yucca Mountain region, $E2$ is the probability that such an event will occur within the repository block, and $E3$ is the probability of exceeding regulatory release limits, given $E1$ and $E2$. The first part the conditional probability represented by equation (1), $E1*E2$, has been described previously[1,2]; it represents the probability of a igneous event penetrating the repository. Guidlines provided in 40 CFR 191 Appendix B state that if R is less than 10^{-8} per year, volcanism may not be a significant licensing issue for the Yucca Mountain site.

The goal of our work is to bound each of the parameters, *E1*, *E2*, and *E3*, in order to provide information for site suitability determinations and for site suitability issues. Below we present preliminary estimates of *E3* for the scenario of a magmatic event intersecting the repository and feeding an eruption. Work in progress is presented to show how we are refining the *E3* calculation for such a case. We also discuss work in progress on understanding *E3* for subsurface processes associated with magmatism. Finally, more general research is presented to understand the physical bases for *E1* and *E2*.

ERUPTIVE EFFECTS

If a magmatic event penetrates the repository and continues to the surface to form a volcanic eruption, it is expected that some repository material will be ejected onto the surface of the mountain. The most likely type of event is a basaltic scoria-cone and lava-flow forming eruption[3]. The maximum erupted volume of magma for such scoria cones in the Yucca Mountain region is 10^8 m^3. We assume that the original mountain surface, before partial burial by ejecta, is the accessible environment from a regulatory perspective. It is most likely that magma would rise through the repository as a near-vertical dike, assuming the shafts and tunnels have been properly backfilled. If backfilling is not complete, or has settled substantially, it is possible that some or all of the magma may be diverted into the shaft and tunnel complex. Any magma that is diverted in this manner is unlikely to reach the surface, and does not play a further role in our analysis of eruptive effects.

In order for waste to be erupted, it must first be entrained into the upward-flowing magma. The process of entrainment is probably quite complex and is not easily treated by theory; our approach instead focusses on data from analog volcanoes. We conservatively assume that radioactive waste in the wall of a dike has the same probability of being entrained as the wall rocks. This is conservative because the waste is actually much denser than the wall rocks, and because during much of the repository lifetime the waste will remain in cannisters and in rod form. The cannisters have lengths that are of the same order as expected dike widths (0.5 - 5.0 m), so that waste entrainment would actually be much less likely than wall rock entrainment. Thus the volume fraction of

erupted wall rock (lithic fragments) in analog volcanoes can be used to provide a conservative estimate of erupted waste.

Dikes can either propagate their own, self-generated fractures, or can follow pre-existing fractures under suitable conditions[4]. Once a fracture is created, magma overpressure pushes the dike walls apart, creating a local compression in the rocks adjacent to the dike[5]. In general the magma does not exhume a volume of wall rock equal to the volume of the dike. Thus we argue that the thickness of the dike does not greatly affect the amount of wall material that is available for entrainment, although we also note that thicker dikes commonly imply larger eruptive volumes (the dike thickness does play a role in *subsurface* effects, though). Dike orientations, based on current extension direction and orientations of preexisting faults, are likely to lie between due N and about N35^{o}E (dike strike). The worst-case scenario would be a dike injected along the long dimension of the repository, which is roughly 3.8 km long and oriented approximately N5^{o}E. Current repository designs have the cannister rows oriented at 45^{o} to the extension direction, in which case it is highly unlikely that a dike could perfectly coincide with a row. The release calculation given below is not sensitive to these considerations.

Previous work[3] has indicated that the maximum volume of lithic fragments in Strombolian scoria cones is about 0.06% of the total pyroclast volume. The total volume of erupted lithics for an eruption with a total volume of 10^8 m^3 would then be 6.0×10^4 m^3. Some fraction of this will actually be derived from the repository horizon.

Lithic fragments can be derived from almost any depth in a dike filled with ascending magma, although they are most likely to be derived from shallow depths where the magma-gas mixture is moving at the highest velocities. For this conservative calculation we will assume that erupted lithic fragments are derived in even proportions from all depths down to the base of the repository (Figure 1a). The thickness of the zone of waste emplacement will be approximately 5 m (the length of vertically-emplaced waste containers), while the average depth to the repository is about 300 m. Thus the repository horizon comprises 1.7% of the total thickness of lithic derivation, implying that about 1020 m^3 of the erupted lithic material will actually be from the repository horizon.

The volume of waste per package is 1.1 m^3; 35,000 containers spread over a repository area of about 5.6×10^6 m^2 would comprise 0.14% of the repository volume. Under these conditions, 1.5 m^3 of waste would be ejected. Note that the number of waste packages intersected at depth may be larger, but only some fraction of these actually travel to the surface and are erupted.

Estimates of regulatory release limits range from one to three waste packages equivalents. The above conservative consequence calculation suggests that release limits might be exceeded under the assumed conditions, implying that $E3 \sim 1.0$.

We are refining the release calculations by studying in detail how wall rock erosion varies as a function of depth in the volcanic plumbing system. Field observations suggest that most conduit erosion occurs within the uppermost few tens of meters in the conduit, to produce a flaring geometry (Figure 1b). If this is the case, the most of the 0.06% proportion of lithic fragments in an eruption will be derived from levels above the repository horizon, which would decrease the calculated value of *E3*. We are taking two approaches to this problem. The first is to look at eroded volcanic centers such as Paiute Ridge (NTS) where basaltic conduits and dikes are exposed by faulting and erosion. This allows us to directly observe the conduit shape as a function of depth as it was during the final phases of the eruptions. The second approach is to study lithic fragments in young scoria cones that erupted through well-characterized basement stratigraphy. One example of this is the Red Cone - Black Cone center in Crater Flat, where a well has been drilled in close proximity. Erupted lithics can be matched to a depth based on the stratigraphy in the well. Other examples we are studying are the San Francisco and Vulcan's Throne volcanic fields in Arizona. These volcanoes erupted through the well-characterized, layer-cake stratigraphy of the Colorado Plateau. Again, the hope is that erupted lithic fragments can be matched to depths of origin, so that erosion as a function of depth can be quantified.

SUBSURFACE EFFECTS

Magmatic events can also affect the repository performance by processes that do not involve actual eruption of waste; any shallow intrusion can have these effects whether or not magma rises all the way to the surface and erupts. Here we consider only intrusive events that occur directly below, in, or above the repository horizon (i.e., within the repository block) as either dikes or sills. Studies to constrain E3 for subsurface effects fall into two categories: (1) effects caused by the thermal influence of magmatic activity (short term effects), and, (2) hydrologic effects caused by the presence of cooled intrusive bodies and the changed hydrologic properties of the host rocks (long term effects).

The first consequence analysis for an igneous intrusion through the repository was attempted during 1990 as part of the performance assessment calculational exercises (PACE-90), coordinated by the Yucca Mountain Site Characterization Project Office. In this analysis, G. Zyvoloski and G. Valentine studied the air convection that results from intrusion of a basaltic dike in the unsaturated zone. In the unsaturated zone, the dike cooling is dominated by thermal diffusion, which is very slow. Pore air convects quite rapidly but only accounts for about 20% of the total cooling. The air convection can, however, carry volatile radionuclides to the accessible environment. It became clear during the analysis that more characterization work is needed to better understand the types of processes that must be accounted for in consequence analyses.

We are now focusing on collecting field data pertaining to the factors that determine intrusion geometry, cooling histories of intrusions, the importance of magmatic volatiles in the resulting hydrothermal systems, contact metamorphism, effects of intrusions on long-term hydrology, and whether the probability of a noneruptive intrusion in the repository block is equal to the probability of an eruption through it. A field area that we have been studying in detail for these purposes is the Paiute Ridge area (eastern Nevada Test Site; Figure 2), where alkali basalts intruded Paintbrush and Timber Mountain tuffs about eight million years ago[3,6,7]. The structural system at Paiute Ridge 8 Ma was a rift, 15-20 km long (N-S) by 4-8 km wide. Basaltic dikes, sills, conduits, and

eruptive products are all exposed within a small area. Because these basalts intruded tuffs that are very similar to those at Yucca Mountain, the contact metamorphic effects can be directly applied to repository problems.

Several important observations have been made at Paiute Ridge. For example, although eruptions apparently occurred only on the floor of the graben, dikes did intrude to shallow depths within the surrounding horst blocks (Figure 3). This observation, especially if it holds true at other locations, may affect the calculation of intrusion probabilities. Most dikes at Paiute Ridge are parallel or coplanar with normal faults that were present during the magmatic activity; this is a common geometric relation and has been noted in other areas in southern Nevada[8]. The exceptions at Paiute Ridge are small dikes that radiate outward from plugs or conduits. Most of the dikes form, along part of their lengths, *en echelon* sets. Some dikes locally fed sills; the thickest sill (~ 50 m) differentiated *in situ* to syenite[7]. Paleomagnetic studies are currently being carried out by J. Geissman (University of New Mexico) to check for multiple intrusive events and for magma emplacement mechanisms.

The host tuffs (mainly bedded Paintbrush Tuffs, and Rainier Mesa member of the Timber Mountain Tuff[6]) were mostly nonwelded prior to emplacement of the intrusions. Heat and stress from the intrusions resulted in various degrees of welding, which requires temperatures in excess of about 600 C depending on the water content of the tuffs and the applied stress; higher temperatures are required for welding of dry tuff[9,10]. Around dikes the maximum degree of welding most commonly occurs in the tuff immediately adjacent to the dike/tuff contact. Welding in such cases is manifested by the presence of flattened pumice fragments, decreased porosity, local development of vitrophyre zones, and increased resistance to erosion compared to unaffected tuff (Figure 4a). Welding effects decrease to zero at distances of 1-5 m from dike margins in most cases, although one example has been found where the maximum welding is offset from the margin by about 0.5 m (Figure 4b); this may be related to interaction between heat and hydrothermal waters. Flattening of pumice fragments produces a fabric or foliation that is parallel to the plane of the dike, a result of the compressive stress exerted by the flowing magma on the wall rocks. Welding adjacent to sills produces subhorizontal foliation. The rocks overlying some of the larger sills at Paiute Ridge sagged over the center parts of the sills. Welding and hydrothermal alteration occurred for several tens of meters above these large sills.

Welding, with loss of porosity and development of foliation, is important from the perspective of consequence analysis. Firstly, it can be used to constrain modeling of the thermal and hydrothermal processes that may affect the repository if an intrusion were emplaced through it or nearby. Welding is sensitive to the presence of hot water, and the degree of welding plus any alteration products can be used to determine the duration of the thermal event and its strength. Hydrothermal processes in the repository horizon could cause rapid corrosion of waste packages and accelerated transport of radionuclides to the accessible environment by either liquid- or vapor-phase transport, as mentioned above. Second, welding alters the hydrologic properties of the rock, so that when the thermal perturbation from an intrusion has decayed away, the new groundwater flow field may be different compared to its pre-intrusion state. The increased competence of the newly welded tuffs may enhance fracture flow, especially with the presence of the welding foliation. Alternatively, loss of porosity may produce a permeability barrier that causes local increases in hydraulic head, resulting in fast paths for migration and accelerated waste package corrosion.

The hydrologic properties of the dike itself may produce important changes in the long term groundwater flow. These properties are poorly known at this time; it is likely that they can vary widely, especially in terms of unsaturated flow properties. If a dike cools to form a relatively competent and intact body that is at a high angle to the direction of groundwater flow, perching may result. A possible example of this is found at Paiute Ridge, where a spring occurs on the upgradient side of a major dike. We are currently investigating whether this perching is caused by the dike itself, or by the presence of a depositional contact between the Paintbrush Tuffs and underlying limestones, or by a combination of both.

ERUPTION AND MAGMA DYNAMICS

The physics of magmatic processes provide important constraints on the overall magmatic system that produces small basaltic centers in the Yucca Mountain region. The data being collected on these centers, including

geochronology, geochemistry, petrology, physical volcanology, and geophysics, provide information on the timing of eruptions, compositional variations, magma source regions, depths of reservoirs, presence of partial melts, volumes of eruptions, and the eruption conditions. All of these factors must be understood in order to have a physical basis for prediction of future behavior.

The Lathrop Wells basaltic center appears to have erupted basalt sporadically since about 150 ka, with the youngest eruptions being as recent as 20 ka[2,11,12,13,14]. The total volume of erupted material at the center is about 5.7×10^7 m^3, so that each eruptive event comprises a relatively small volume. An aspect that is important to understand is the mechanisms by which these small volumes of magma erupt within such a focused area. The time between eruptions (probably on the order of 10^4 years) is much longer than characteristic cooling times of the feeder dikes (a few days to weeks), so it seems unlikely that each event follows the path of previous events as a result of thermal memory. The erupted magmas are mostly free of phenocrysts, but geochemical evidence suggests that significant fractionation must have taken place in the magma reservoir(s) at depths of about 30 km[12]. Isotopic evidence suggests that there have been at least two separate batches of magma[12]. We are currently studying the dynamics of small volume basaltic magma chambers by numerical simulation with the goal of gaining an understanding of these observations.

Magma Chamber Modeling

The first scenario that we are modeling is that of a small basaltic sill emplaced into cool country rock. Dimensions of 10 m thickness by 30 m wide were chosen for a cross section based on dimensions of sills at Paiute Ridge, where excellent exposures of sills allow us to directly check the field implications of the modeling. Because the modeled sill is much longer than it is wide, we are able to carry out computations in two dimensions. The governing equations for this system and a brief description of the numerical solution technique are given in Appendix A. Magma viscosity is strongly temperature dependent; we use a viscosity function that accounts for the effects of crystals on the viscosity[15]. For our initial studies (Figure 5), the viscosity of all the magma in the chamber depends on the maximum temperature in the chamber at a given time. Studies in progress are modeling the full local temperature dependence of viscosity, plus effects of melting and crystallization.

One of our first calculations show many of the important features of convection in chambers that are surrounded by initially cool rock (Figure 5). Heat diffuses through the thick wall very slowly, which has an important effect on convection. Initially the chamber can be thought of as two parts: the bottom half, which is dynamically stable (cooler, denser on the bottom), and the top half, which is unstable (cooler, denser on the top). After initial emplacement, the magma first cools through the thermal boundary layer along its contact with the country rock. As the boundary layer thickens, the part along the roof and sidewalls becomes unstable and forms downwelling plumes, while the boundary layer along the bottom contact simply grows by thermal diffusion. In conventional convection studies the bottom boundary is maintained at a constant, high temperature and the top at a low temperature, and plumes or convection cells generally penetrate the entire thickness of the chamber. In the example in Figure 5, however, the plumes carry cool fluid downward from the top boundary until they reach the level in the bottom boundary layer where the local temperature equals the temperature at the core of the plume. At that level the plume spreads out laterally and adds material to the bottom boundary layer. Actually, each plume has its own thermal structure with the coolest fluid being in the plume core, and an increasing temperature toward the edge of the plume. As a fluid in the plume enters the bottom boundary layer the outer margins of the plume begin to spread laterally at higher levels than the core of the plume, each part spreading at the level where the local temperature equals the temperature of that part of the plume.

Conventional convection studies with constant boundary temperatures (bottom hotter than top) produce both downwelling and upwelling plumes, which together can form convective cells. In the configuration described above (Figure 5) the downwelling plumes enter a stably stratified environment in the bottom half of the magma chamber. A characteristic of stably stratified fluids is that vertical mixing is retarded. Thus the plumes merely spread out at their neutral density levels and quietly add to the stable portion of the chamber, which grows at the expense of the upper, unstable portion. Some upward flow does occur in the upper part of the chamber, between the center and wall plumes, but it is very weak and diffuse. It is expected that most crystallization would take place *in situ* within the bottom stable part of the chamber, and along the side and top contacts. We are currently working on modeling this system with crystallization fully accounted for and with a wide range of

physical dimensions. Understanding these systems will provide insight into how cooling/crystallization processes may act to trigger eruptions in the Yucca Mountain region.

Eruption Dynamics Modeling

Another important set of observations that can be used to constrain eruption and magma dynamics is the facies distribution of the volcanic deposits. Basaltic volcanoes at Crater Flat have produced both lava flows and pyroclastic material[3], the latter forming the main cone constructs and more widespread fallout sheets. These facies, or types of deposits, are produced by eruptions of gas and magma clots. The eruptions may take the form of relatively steady jets and fountains (Hawaiian eruptions), or of intermittent or frequently-repeated bursts of material that form short-lived fountains and ballistically ejected bombs (Strombolian eruptions). The development of a given facies depends on the local rate of accumulation of clasts and their temperature[16] (Figure 6). The *distribution* of facies, which reflects the spatial variations in accumulation rate and temperature, depends on the eruption dynamics, namely, the magma discharge rate, volatile content, vent radius, and clast size.

We are carrying out two-phase flow modeling of basaltic pyroclastic eruptions. To date we have studied a suite of conditions for Hawaiian style eruptions. The model computes the flow of gas with dispersed particles. The particles and gas are coupled together by drag (momentum exchange) and heat exchange terms, but otherwise their relative motion is independent. The model equations and description of the numerical technique are given in Appendix B.

Two approaches have been used to determine appropriate eruption conditions. The first approach is determined by theoretical analysis of the ascending flow in the volcanic conduit[17]. This conduit analysis assumes that the gas and liquid magma phases are in thermal equilibrium and that their velocities are equal (the *homogeneous flow* approximation), and that the pressure in the conduit is equal to the local lithostatic pressure[17,18]. Eruption conditions, determined by the homogeneous conduit flow theory, are shown for the four runs discussed here in Table 1. Basaltic eruptions, however, commonly are not characterized by homogeneous flow in the conduit because of significant relative motion between the gas and liquid phases[19,20];

this is especially true for Strombolian eruptions, which are caused by the coalescence and rise of large gas bubbles through the magma column. Thus we also model eruption conditions that are based on magma discharge rate, vent size, and clast velocity, with the velocity and mass fraction of the gas at the vent being dependent variables (in the homogeneous flow treatment, the gas content is an independent variable); this modeling is not discussed here.

Run 8 (Figure 7) has a mass discharge rate, vent radius, and volatile content that was observed during some relatively less energetic fountaining phases of the 1984 eruptions of Puu Oo vent, Kilauea, Hawaii[21]. This simulation thus serves as a useful validation experiment. Simulated fountain height (70-80 m) compares quite well with observations of fountain height at Puu Oo during some of the weaker eruptive events. The accumulation rate, obtained by multiplying the clast volume fraction by the downward clast velocity at the bottom of the computational mesh, varies with radial distance from the vent (Figure 8) in a manner that also compares well with observations. Maximum accumulation rate occurs at a distance of about 35-40 m from the vent center, and decays rapidly to zero at a distance of 80 m. For an eruption that is sustained at these conditions, the highest point on the crater rim would be located at the radius of maximum deposition, producing a crater of 70-80 m diameter, and the entire cone would be about 160 m in diameter, although in reality these dimensions may be larger due to avalanche processes that sustain the cone slopes at angles less than or equal to the angle of repose. For comparison, the crater at Puu Oo had a diameter of about 100 m and the cone diameter was about 350 m by the end of the eruptions in 1984[21], but it is important to note that the cone-forming eruptions had a wide range of conditions and occasionally produced fountains of 400 m height, which can easily account for the differences between simulated and natural results in this case (fountain heights are the only true *real time* data that we have on the eruption dynamics). Temperature of depositing clasts is highest (~ 1000 C) at a distance of 30 m, and decreases to about 600 C at the outer margin of deposition (Figure 8). At Puu Oo, the depositing clasts were hot enough on the inner slopes of the crater to coalesce and feed lava flows, those on the upper parts of the cone slopes were sufficiently hot to weld and locally formed rootless lava flows (Figure 7), while the outermost slopes are comprised mainly of loose scoria. These facies compare well with the simulated temperature variations. Overall, we feel that when the complexity of the natural eruptions are considered, the simulations are fairly accurate and compare well with nature.

Another set of observations that can be used for validation are those related to general cone morphology. The average ratio of crater diameter to cone diameter is about 0.4, based on a survey of 910 cones worldwide[22]. Inspection of accumulation rate *versus* radial distance for the four runs discussed here (Figures 8, 9), shows that maximum accumulation does indeed occur at distances of about 0.4 of the distance to the outer limit of accumulation. It is important to point out that the results of the simulations can only be applied to *facies variations within single deposits (layers) that were produced by a single combination of eruption conditions*. Comparison of simulation results with a given set of conditions will rarely apply to an entire cone construct because most cones are built from many eruptive episodes with varying conditions, and are subjected to other processes such as hydrovolcanic explosions.

Run 3 has an exit velocity that is similar to run 8, but its magma discharge rate is an order of magnitude larger. This implies a much lower volatile content (Table 1). The maximum accumulation rate for run 3 is nearly two orders of magnitude higher than that for run 8, but because of the similar velocities the location of maximum accumulation is nearly identical for the two runs (Figure 8). The clast temperature in run 3 is relatively low because of the lower simulated eruption temperature, but unlike the other three simulations temperature decays more slowly out to intermediate distances (~ 50 m), and beyond which the decay is more dramatic. In the geologic record this type of eruption would most likely be represented as cones where material that fell into the inner crater and the proximal outer slopes would coalesce and flow away as lava, and only the outermost slopes of partially welded and loose scoria would remain as the cone.

Run 4 has a much higher velocity and a higher discharge rate than runs 3 and 8, but also has a relatively high volatile content (Table 1). It produces a relatively high fountain that disperses pyroclasts over a wider area (Figure 8). Because the clasts have relatively long travel times in the fountain, they are relatively cool by the time they are deposited. Although the maximum accumulation rate is high (~ .04 m/s at 80 m from the vent center), the low temperature of the clasts will likely prevent any welding or coalescence, producing a deposit that consists almost entirely of loose scoria.

The conditions of run 4 were duplicated for run 9, except that the latter has coarser pyroclast size and higher temperature (Table 1). The larger particles in run 9 are less affected by gas flow field, and are able to follow paths that are more nearly ballistic than those in run 4. The result is an offset of the maximum accumulation distance, away from the vent relative to run 4 (Figure 9). The higher eruption temperature and larger particle size in run 9 produces relatively hotter deposits, which may weld. Compared to runs 3 and 8, deposits from runs 4 and 9 have more gradual variations in accumulation rate and temperature with increasing distance from vent, an effect that is mainly due to the differences in eruption velocities.

These are only initial results, but the possible applications of this modeling are important and exciting. More simulations over a wider range of conditions, plus quantification of the influence of accumulation rate and temperature on deposit facies, will allow us to constrain eruption conditions at scoria cones based on the distribution of these facies. For example, the most recent eruption of A-cone at the Cima volcanic field produced a cone with loose scoria on the outer slopes, welded spatter on the crater slopes, and an aa lava flow. The presence of the aa flow implies discharge rates in excess of $3x10^4$ kg/s[23], and the pyroclastic facies variations suggest a discharge rate on the order of 10^5 kg/s, based on the above simulations. The main cone at Lathrop Wells consists almost entirely of loose scoria, which would suggest relatively higher discharge rates, although sparse bombs on the crater rim suggest that the eruption may have closed with a brief Strombolian phase. Small aa flows around the Lathrop Wells cone indicate discharge rates in excess of $3x10^4$ kg/s, but these must have been very short lived eruptions to produce flows of such limited extent. This type of information will be very useful in understanding the overall magma dynamics system at Crater Flat.

SUMMARY

We have reported on work in progress related to constraining both *E1* (probability of eruption) and *E3* (consequences). Consequence analysis for eruptive effects is being addressed mainly by studies of the lithic

distributions in analog volcanoes. Consequence analysis of subsurface effects is being addressed by studies at analog sites such as Paiute Ridge, which will be combined with modeling. Understanding the overall magma-dynamic system is important for providing a physical basis for prediction of future behavior. To date we have begun magma chamber studies with small sill geometries. Eruption modeling based on multiphase flow is being used to constrain magma discharge rates and volatile contents. Taken together and combined with other volcanism research being carried out, these different approaches will provide a comprehensive understanding of volcanism in the Yucca Mountain region and its possible impacts on the proposed repository.

APPENDIX A - MAGMA CHAMBER MODEL

The governing equations and numerical solution technique for our magma chamber model have been developed and reported in the literature by B.J. Travis (Los Alamos National Laboratory)[24,25]. The governing equations are:

$$\nabla \cdot \mathbf{u} = 0 \quad , \tag{A-1}$$

$$\nabla^2 \cdot \mathbf{u} = \nabla P - Ra\, T\mathbf{z} \quad , \tag{A-2}$$

$$\frac{\partial T}{\partial t} + (\mathbf{u} \cdot \nabla) T = \nabla^2 T \quad , \tag{A-3}$$

where $\mathbf{u}$ is the velocity, P is pressure, T is temperature, $\mathbf{z}$ is the unit vertical vector, t is time. The Rayleigh number, Ra, is defined by

$$\frac{\beta g\, \Delta T\, D^3}{\kappa \nu} \quad , \tag{A-4}$$

where β is the isobaric thermal expansion coefficient, g is the magnitude of the gravitational acceleration, ΔT is a characteristic temperature difference which occurs over a distance D, κ is the thermal diffusivity, and ν is the kinematic viscosity. Equation A1-1 is conservation of mass for the incompressible fluid. Equation A1-2 is conservation of momentum using the standard Boussinesque approximation. Equation A1-3 is conservation of specific internal energy, which can be expressed in terms of temperature for incompressible flow. These equations also incorporate the assumption of infinite Prandtl number, which is appropriate for magmatic convection problems.

The finite-difference numerical solution to these equations is laid out in Ref. 25, and will not be repeated in detail here. The finite difference grid for the calculation shown here (carried out by B. Travis and G. Valentine) includes 60 zones within the fluid part of the domain. This is ample resolution for this scenario, which has an initial Rayleigh number of about 10^8, based upon the half thickness of the "sill" and ΔT defined as the initial magmatic temperature minus the solidus temperature. Velocity was held at zero for the part of the domain that is outside the fluid region, thus allowing only thermal diffusion in that part.

For the simulation discussed in the text (Figure 5), the following material properties were used: $\beta = 6.0 \times 10^{-5}$ / °C, reference density at 800 °C of 2750 kg/m^3, and $\kappa = 8.0 \times 10^{-6}$ m^2/s. The temperature dependent kinematic viscosity is given by

$$\nu = 0.1\left[11.02 - \frac{1.2 \times 10^4}{T}\right]^{-2.5} \text{ m}^2/\text{s} \quad , \qquad \text{(A-5)}$$

a formulation that accounts for the effects of crystals on bulk viscosity. This relationship is valid between temperatures of about 1090 °C and the liquidus temperature. Below 1090 °C the magma is so crystal rich that it behaves as a solid on the time scale of magmatic flow phenomena. These properties and relationships can be found in Refs. 15, 27, 28.

Although not listed in the equations above, compositional variations and their effects on flow (i.e., double diffusive convection) can also be included[24]; such effects are important in magmatic processes[26] and will be accounted for as our study progresses.

APPENDIX B - TWO-PHASE FLOW ERUPTION MODEL

The approach used here to model eruptive jets, fountains, and plumes is to solve the full set of two-phase, compressible Navier-Stokes equations[29] for injection of a hot, particle-laden gas into a cool atmosphere. Each phase is modeled as a continuum, one of the phases being compressible (the vapor phase), and the other being incompressible (the particles or magma clots). The two continua occupy the same space, but all transport quantities are multiplied by the volume fraction of the relevant phase. The equations are:

$$\frac{\partial}{\partial t}(\theta_s\rho_s) + \nabla\cdot(\theta_s\rho_s\mathbf{u}_s) = 0 \quad , \tag{B-1}$$

$$\frac{\partial}{\partial t}(\theta_g\rho_g) + \nabla\cdot(\theta_g\rho_g\mathbf{u}_g) = 0 \quad , \tag{B-2}$$

$$\frac{\partial}{\partial t}(\theta_s\rho_s\mathbf{u}_s) + \nabla\cdot(\theta_s\rho_s\mathbf{u}_s\mathbf{u}_s) = -\theta_s\nabla p + K_s(\Delta\mathbf{u}) + \theta_s\rho_s\mathbf{g} - \nabla\cdot\tau_s \, , \tag{B-3}$$

$$\frac{\partial}{\partial t}(\theta_g\rho_g\mathbf{u}_g) + \nabla\cdot(\theta_g\rho_g\mathbf{u}_g\mathbf{u}_g) = -\theta_g\nabla p + K_g(\Delta\mathbf{u}) + \theta_g\rho_g\mathbf{g} - \nabla\cdot\tau_g \, , \tag{B-4}$$

$$\theta_s\rho_s\left[\frac{\partial I_s}{\partial t} + \nabla\cdot(I_s\mathbf{u}_s) - I_s\nabla\cdot\mathbf{u}_s\right] = R_s - \tau_s:\nabla\mathbf{u}_s \quad , \tag{B-5}$$

$$\theta_g\rho_g\left[\frac{\partial I_g}{\partial t} + \nabla\cdot(I_g\mathbf{u}_g) - I_g\nabla\cdot\mathbf{u}_g\right] = -p\nabla\cdot(\theta_g\mathbf{u}_g + \theta_s\mathbf{u}_s) + R_g + |K_g|(\Delta\mathbf{u})^2 - \tau_g:\nabla\mathbf{u}_g \, , \tag{B-6}$$

where θ is volume fraction, ρ is material density, $\mathbf{u}$ is the velocity vector, p is gas pressure, K is interphase momentum exchange (drag), $\Delta\mathbf{u}$ is the slip velocity between the two phases, $\mathbf{g}$ is gravitational acceleration, τ is the strain rate tensor, I is specific internal energy, and R is interphase heat exchange. The subscripts s and g refer the above variables to the solid (particle, droplet) or gas phase, respectively. The strain rate tensor has been presented and discussed in detail elsewhere[30,31]; it incorporates a mixing-length model for turbulence.

These coupled partial differential equations are solved using an explicit finite difference scheme that is a simplification of the *implicit multifield flow* technique[29]. The simulations discussed in this paper are based on two-dimensional, axisymmetric solution of the above equations. The finite difference grid uses cell dimensions ranging from 1 m to 200 m, depending upon the scale of the problem of interest; the simulations presented here used dimensions ranging from 5 m to 20 m. The method has proven valuable for modeling many explosive eruptive phenomena[30-34].

The following equations of state and constitutive relations are employed:

$$I_s = c_{vs}T_s \qquad \text{(B-7)}$$

$$I_g = c_{vg}T_g \qquad \text{(B-8)}$$

$$p = (\gamma - 1)\rho_g I_g \qquad \text{(B-9)}$$

$$\theta_g = 1 - \theta_s \qquad \text{(B-10)}$$

$$K_g = -K_s \qquad \text{(B-11)}$$

$$R_g = -R_s \qquad \text{(B-12)}$$

$$K_s = \frac{3\theta_s \rho_g c_d}{16 r_s} |\Delta u| \qquad \text{(B-13)}$$

$$R_s = \frac{-3\theta_s \varepsilon}{r_s}\left[e_s T_s^4 - a_g T_g^4\right] - \frac{3\theta_s k_g}{2r_s^2}\left[2.0 + 0.6(Ry_s^{1/2} Pr_g^{1/3}\right]\Delta T \qquad \text{(B-14)}$$

$$Ry_s = \frac{2 r_s |\Delta u|}{\nu_g} \qquad \text{(B-15)}$$

$$Pr_g = \frac{c_{pg} \rho_g \nu_g}{k_g} \qquad \text{(B-16)}$$

$$\Delta T = T_s - T_g \qquad \text{(B-17)}$$

where c_v is the specific heat at constant volume, T is temperature, γ is the ratio of specific heats for the gas (here assumed to be 1.33, for steam), c_d is the coefficient of drag between particle and gas (here taken to be ~ 1.0), r_s is the particle radius, $|\Delta u|$ is the absolute value of the slip velocity, ε is the Stefan-Boltzmann constant for radiative transfer, e_s is the infrared emissivity of the particles, a_g is the infrared absorptivity of the gas, k_g is the thermal conductivity of the gas, ν_g is the kinematic viscosity of the gas, and c_{pg} is the specific heat at constant pressure for the gas. Equations B-7,8 relate the specific internal energies to temperatures, assuming constant specific heats. Equation B-9 is the ideal gas equation of state, using the properties of steam at high temperature. Equation B-13 is the drag function whereby momentum is transferred between the two phases. Equation B-14 is the interphase heat transfer term, including radiative and convective terms. Material properties and implications of these equations are discussed in detail in Ref. 30.

ACKNOWLEDGMENTS

This work was supported by the Yucca Mountain Site Characterization Project Office as part of the Civilian Radioactive Waste Management Program, with the exception of the magma chamber simulation, which is supported by Laboratory Directed Research and Development funds at Los Alamos National Laboratory. Non-referenced field data can be found in Los Alamos National Laboratory notebook TWS-EES-5-5-91-08. Computations were carried out in a prototyping mode. The software used for these calculations was not verified, validated, or otherwise subjected to the controls of a quality assurance program that is approved by the Yucca Mountain Site Characterization Project Office. The authors thank K.H. Birdsell for reviewing the manuscript.

REFERENCES

1. B.M. Crowe, M.E. Johnson, R.J. Beckman, "Calculation of the probability of volcanic disruption of a high-level radioactive waste repository within southern Nevada, U.S.A.," *Radioactive Waste Management and the Nuclear Fuel Cycle, 3*, 167-190, 1982.

2. B.M. Crowe, G.A. Valentine, F.V. Perry, "Recurrence rate models of volcanic events: Applications to volcanic risk assessment for the Yucca Mountain Project," this volume.

3. B.M. Crowe, S. Self, D. Vaniman, R. Amos, F.V. Perry, "Aspects of potential magmatic disruption of a high-level radioactive waste repository in southern Nevada," *Journal of Geology, 91*, 259-276, 1983.

4. P.T. Delaney, D.D. Pollard, J.I. Ziony, E.H. McKee, "Field relations between dikes and joints: Emplacement processes and paleostress analysis," *Journal of Geophysical Research, 91*, 4920-4938, 1986.

5. T. Parsons, G.A. Thompson, "The role of magma overpressure in suppressing earthquakes and topography: Worldwide examples," *Science, 253*, 1399-1402, 1991.

6. F.M. Byers Jr., H. Barnes, "Geologic map of the Paiute Ridge Quadrangle, Nye and Lincoln Counties, Nevada," *U.S. Geological Survey Quadrangle Map GQ-577*, 1967.

7. F.V. Perry, "Differentiation of the Paiute Ridge alkaline intrusion, southern Great Basin, Nevada," Los Alamos National Laboratory manuscript, 1982.

8. E.I. Smith, D.L. Feuerbach, T.R. Naumann, J.E. Faulds, "The area of most recent volcanism near Yucca Mountain, Nevada: Implications for volcanic risk assessment," *Proceedings, High Level Radioactive Waste Management, vol. 1*, 81-90, 1990.

9. I. Friedman, W. Long, R.L. Smith, "Viscosity and water content of rhyolite glass," *Journal of Geophysical Research, 68*, 6523-6535, 1963.

10. J.R. Riehle, "Calculated compaction profiles of rhyolitic ash-flow tuffs," *Geological Society of America Bulletin, 84*, 2193-2216, 1973.

11. S.G. Wells, L.D. McFadden, C.E. Renault, B.M. Crowe, "Geomorphic assessment of late Quaternary volcanism in the Yucca Mountain area, southern Nevada: Implications for the proposed high-level radioactive waste repository," *Geology, 18*, 549-553, 1990.

12. F.V. Perry, "Waning magmatism and polycyclic volcanism at Crater Flat, Nevada," this volume.

13. B.M. Crowe, "Basaltic volcanic episodes of the Yucca Mountain region," *Proceedings, High Level Radioactive Waste Management, vol. 1*, 65-73, 1990.

14. B. Crowe, C. Harrington, L. McFadden, F. Perry, S. Wells, B. Turrin, D. Champion, "Preliminary geologic map of the Lathrop Wells volcanic center, " *Los Alamos National Laboratory Report LA-UR-88-4155*, 1988.

15. H.E. Huppert, R.S.J. Sparks, "Melting the roof of a chamber containing a hot, turbulently convecting fluid," *Journal of Fluid Mechanics, 188*, 107-131, 1988.

16. J.W. Head III, L. Wilson, "Basaltic pyroclastic eruptions: Influence of gas-release patters and volume fluxes on fountain structure, and the formation of cinder cones, spatter cones, rootless flows, lava ponds and lava flows," *Journal of Volcanology and Geothermal Research, 37*, 261-271, 1989.

17. L. Wilson, J.W. Head III, "Ascent and eruption of basaltic magma on the Earth and Moon," *Journal of Geophysical Research, 86*, 2971-3001, 1981.

18. J.W. Head III, L. Wilson, "Lava fountain heights at Puu Oo, Kilauea, Hawaii: Indicators of amount and variations of exsolved magma volatiles," *Journal of Geophysical Research, 92*, 13715-13719, 1987.

19. S. Vergniolle, C. Jaupart, "Separated two-phase flow and basaltic eruptions," *Journal of Geophysical Research, 91*, 12842-12860, 1986.

20. S. Vergniolle, C. Jaupart, "Dynamics of degassing at Kilauea volcano, Hawaii," *Journal of Geophysical Research, 95*, 2793-2809, 1990.

21. E.W. Wolfe, M.O. Garcia, D.B. Jackson, R.Y. Koyanagi, C.A. Neal, A.T. Okamura, "The Puu Oo eruption of Kilauea volcano, episodes 1-20, January 3, 1983, to June 8, 1984," *U.S. Geological Survey Professional Paper 1350*, 471-508, 1987.

22. C.A. Wood, "Morphometric evolution of cinder cones," *Journal or Volcanology and Geothermal Research*, 7, 387-413, 1980.

23. S.K. Rowland, G.P.L. Walker, "Pahoehoe and aa in Hawaii: Volumetric flow rate controls the lava structure," *Bulletin of Volcanology*, *52*, 615-628, 1990.

24. B.J. Travis, "Numerical models of 2-D and 3-D geophysical convection," in *Heat Transfer in Earth Science Studies*, C. Carrigan and T.Y. Chu (eds.), HTD-vol. 149, American Society of Mechanical Engineers, p. 23-28, 1990.

25. B. Travis, P. Olson, G. Schubert, "The transition from two-dimensional to three-dimensional planforms in infinite-Prandtl-number thermal convection," *Journal of Fluid Mechanics*, *216*, 71-91, 1990.

26. G.A. Valentine, "Magma chamber dynamics," *Encyclopedia of Earth System Science*, vol. 3, in press.

27. T. Murase, A.R. McBirney, "Properties of some common igneous rocks and their melts at high temperatures," *Geological Society of America Bulletin*, *84*, 3563-3592, 1973.

28. C.M. Oldenburg, F.J. Spera, D.A. Yuen, G. Sewell, "Dynamic mixing in magma bodies: Theory, simulations, and implications," *Journal of Geophysical Research*, *94*, 9215-9236, 1989.

29. F.H. Harlow, A.A. Amsden, "Numerical calculation of multiphase fluid flow," *Journal of Computational Physics*, *17*, 19-52, 1975.

30. G.A. Valentine, K.H. Wohletz, "Numerical models of Plinian eruption columns and pyroclastic flows," *Journal of Geophysical Research*, *94*, 1867-1887, 1989.

31. K.H. Wohletz, G.A. Valentine, "Computer simulation of explosive volcanic eruptions," in *Magma Storage and Transport*, M. Ryan (ed.), John Wiley Publishing Co., p. 114-135, 1990.

32. G.A. Valentine, K.H. Wohletz, "Environmental hazards of pyroclastic flows determined by numerical models," *Geology, 17*, 641-644, 1989.

33. G.A. Valentine, K.H. Wohletz, S.W. Kieffer, "Sources of unsteady column dynamics in pyroclastic flow eruptions," *Journal of Geophysical Research, 96*, in press, 1991.

34. G.A. Valentine, K.H. Wohletz, S.W. Kieffer, "Effects of topography on facies and compositional zonation in caldera-related ignimbrites," *Geological Society of America Bulletin, 104*, in press, 1992.

FIGURE CAPTIONS

Figure 1. Schematic cross sections showing hypothetical eruption of basalt from a dike that penetrates the repository, with lithics being derived in equal proportions from all levels between the repository and the surface (a), or lithic derivation concentrated in the upper few meters of the dike or conduit (b).

Figure 2. Simplified geologic map of the Paiute Ridge area, emphasizing basaltic rocks[6]. Pzu - Paleozoic basement rocks (mainly carbonates), undivided; Tpu - Paintbrush tuffs, undivided; Tmu - Timber Mountain tuffs, undivided (includes Rainier Mesa and Ammonia Tanks members); Qac - Quaternary alluvium and colluvium.

Figure 3. Cross section through Paiute Ridge area (A-A' in Figure 2), showing present day topography and geology, with inferred topography at the time of basaltic activity in lighter lines. Dikes are extrapolated to original depths based on modern exposures off the plane of the cross section. Tpi - Paintbrush tuffs; Tmr - Rainier Mesa member of Timber Mountain Tuff; Tma - Ammonia Tanks member of Timber Mountain Tuff.

Figure 4. Schematic sketch of typical basaltic dike at Paiute Ridge showing effects on the wallrock tuffs (a), and field sketch of basaltic dike where maximum wallrock welding is offset from the dike margin (b).

Figure 5. Two snapshots of the temperature field of a small basaltic magma body, emplaced into country rock at time t = 0. The initial magma temperature is 1200 C, while the initial country rock temperature is 200 C. Two-dimensional time-dependent conduction of heat through the country rock is also computed, but is not shown in these snapshots. The magma viscosity is dependent on the maximum temperature in the domain at a given time. At $t = 5.688 \times 10^{-4}$ years, a downwelling plume is just forming at the center of the roof; downwelling plumes are

also present along the two vertical walls, although they do not show on these plots. By $t = 2.738 \times 10^{-3}$ years, the plumes from the sidewalls and roof center are well-developed and are gradually adding to a growing stable layer at the base of the chamber. The stable base continues to grow at the expense of the unstable top.

Figure 6. Schematic diagram showing the dependence of pyroclastic facies types on local accumulation rate and clast temperature, modified from Ref. 16.

Figure 7. Snapshots of clast volume fraction at 2.5 s (a) and 45 s (b) after initiation of run 8, showing initial rise of clast-laden jet. The simulations are axisymmetric half-spaces, with the left side of the domain being the symmetry axis. The bottom boundary is a free-slip boundary; the top and right boundaries have zero gradient (outflow) conditions. The vertical and horizontal axes are each 700 m long. By 45 s a fountain structure has developed within the lowermost three contours, and a low concentration plume is rising buoyantly above the fountain (the innermost contour represents a particle volume fraction of about 10^{-3}, with each contour representing an order of magnitude decrease moving away from the lower left corner). Also shown are clast temperature contours at 45 s (c), with the innermost contour representing a temperature of 1423 K, and the outermost representing 300 K.

Figure 8. Deposit accumulation rate (top) and clast temperature (bottom) as functions of radial distance from vent center for Runs 3, 4, and 8 (see Table 1).

Figure 9. Deposit accumulation rate and clast temperature for runs 4 (solid lines) and 9 (dashed lines), as functions of radial distance from vent center.

Table 1. Eruption conditions for simulations.

Run No.	velocity (m/s)	temp. (K)	H_2O (%)	vent rad. (m)	clast dia. (cm)	discharge rate (kg/s)
3	33.0	1200	0.06	10	1.0	3×10^6
4	140.0	1200	0.50	20	1.0	1×10^7
8*	32.0	1423	0.50	10	1.0	3×10^5
9	140.0	1423	0.50	20	3.0	1×10^7

* Similar to Puu Oo conditions.

(a)

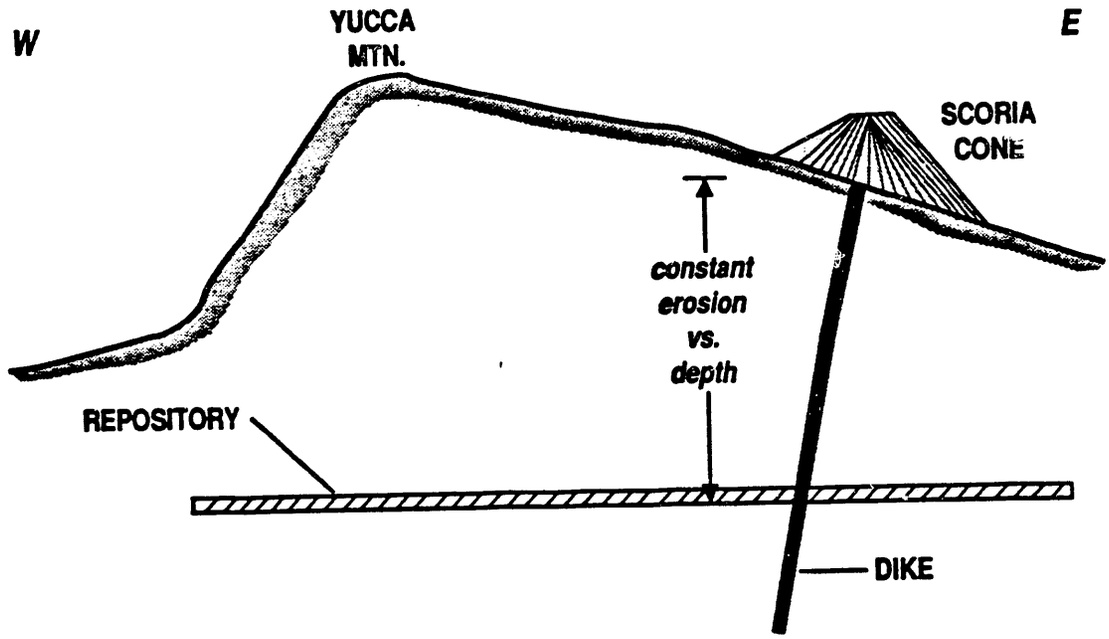
W
YUCCA MTN.
E
SCORIA CONE
constant erosion vs. depth
REPOSITORY
DIKE

(b)

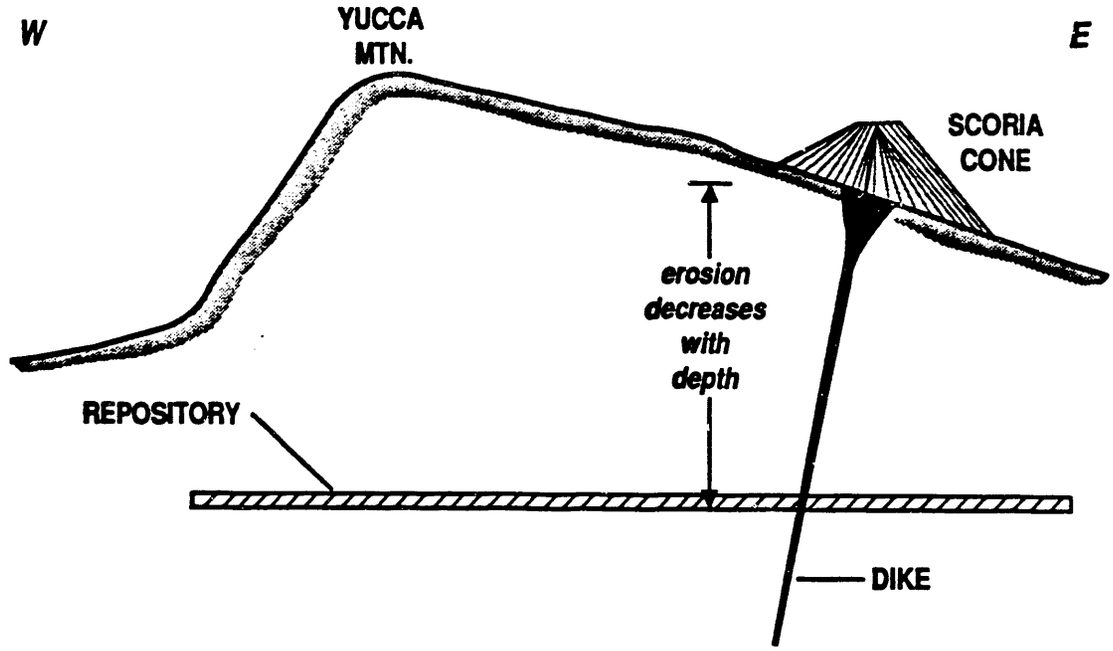
W
YUCCA MTN.
E
SCORIA CONE
erosion decreases with depth
REPOSITORY
DIKE

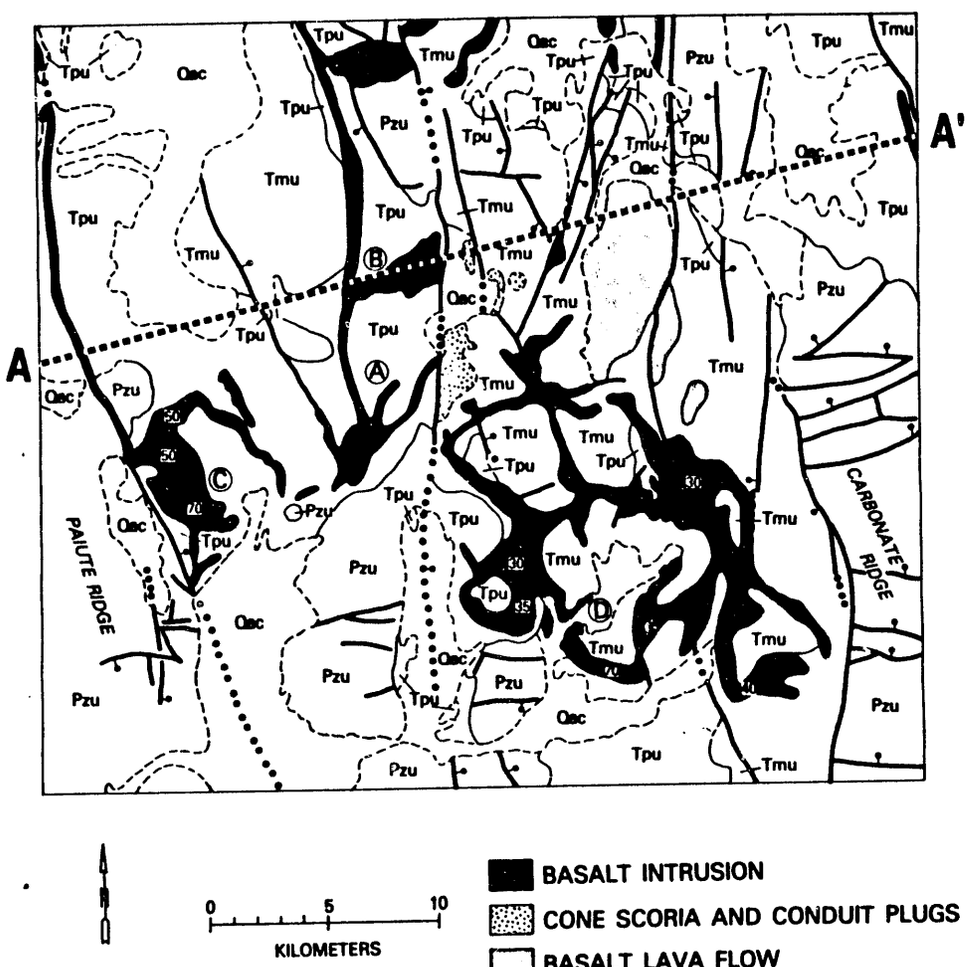
A
A'
B
A
C
D
Tpu
Tmu
Qsc
Pzu
PAIUTE RIDGE
CARBONATE RIDGE
0
5
10
KILOMETERS
BASALT INTRUSION
CONE SCORIA AND CONDUIT PLUGS
BASALT LAVA FLOW

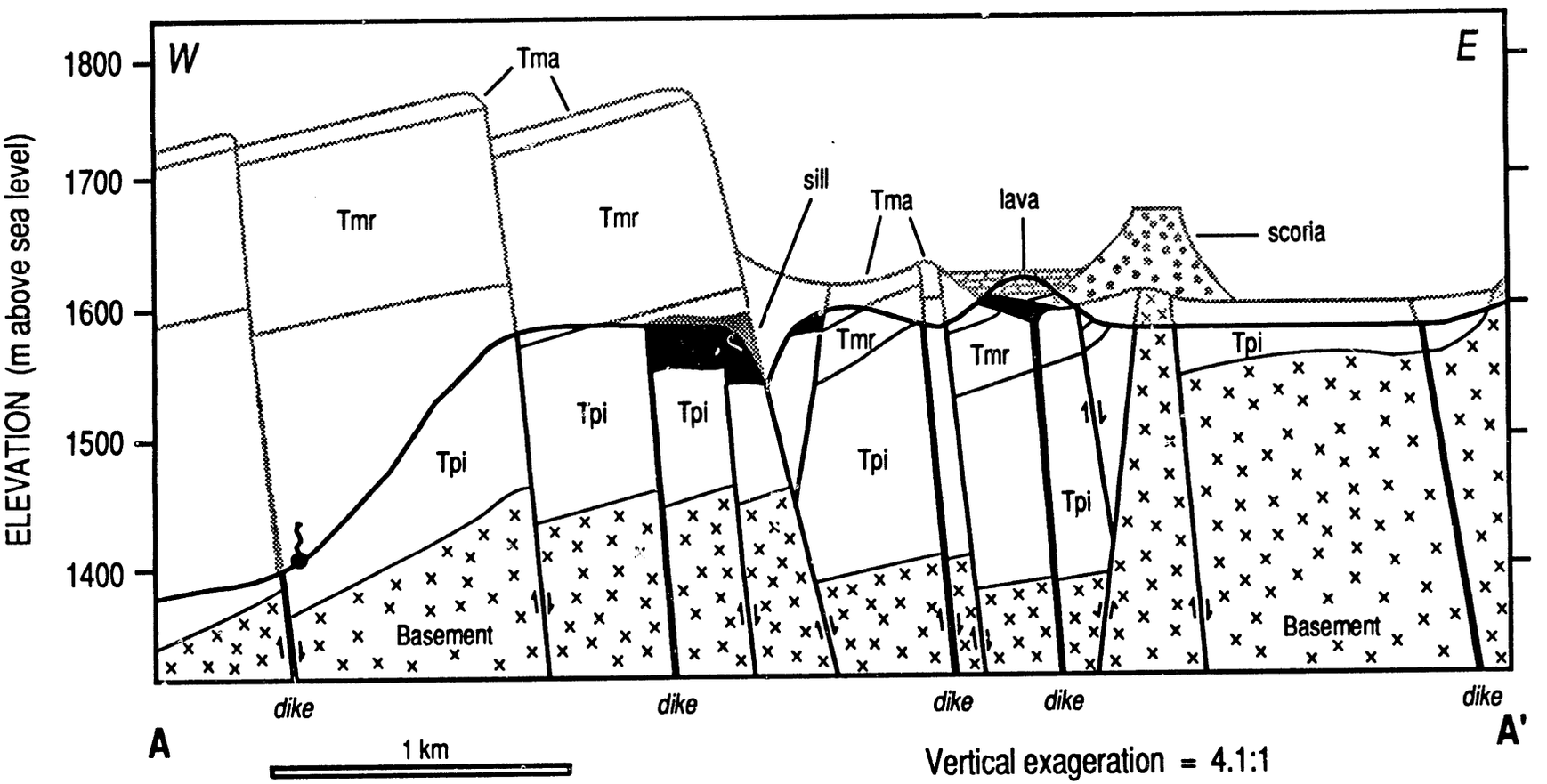
ELEVATION (m above sea level)
1800
1700
1600
1500
1400
W
E
Tma
Tmr
Tmr
sill
Tma
lava
scoria
Tmr
Tmr
Tpi
Tpi
Tpi
Tpi
Tpi
Tpi
Basement
Basement
dike
dike
dike
dike
dike
A
A'
1 km
Vertical exageration = 4.1:1

(a)

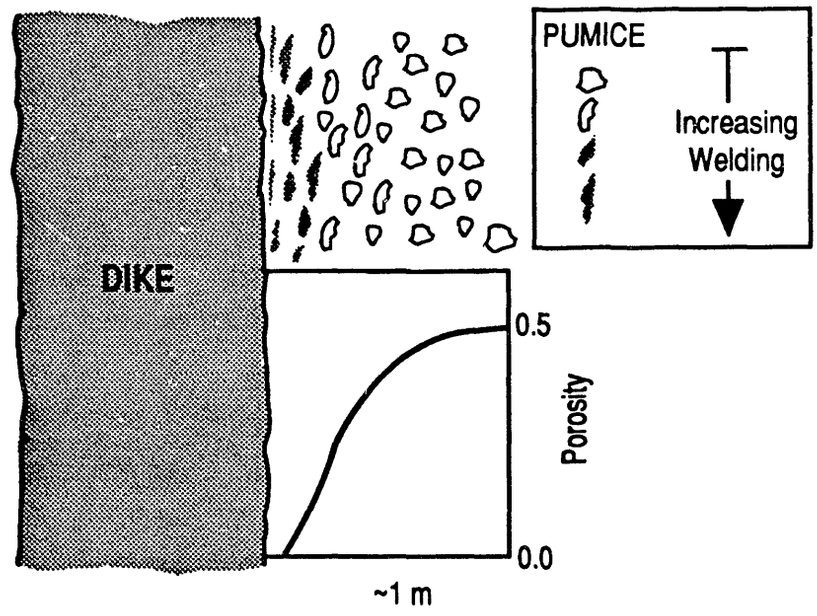
PUMICE
Increasing
Welding
DIKE
0.5
Porosity
0.0
~1 m

(b)

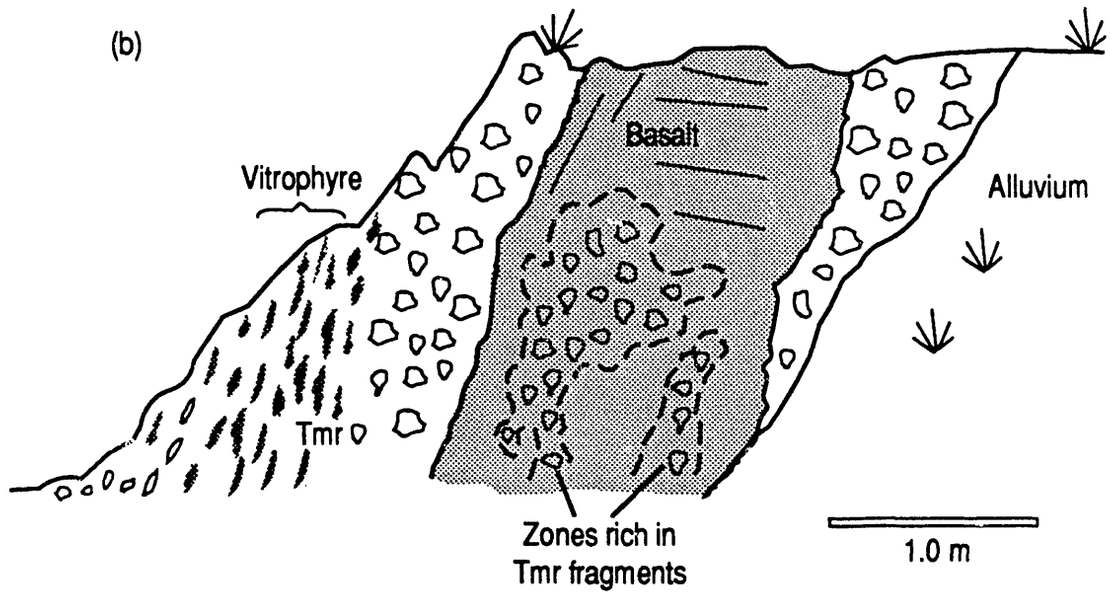
Basalt
Vitrophyre
Alluvium
Tmr
Zones rich in
Tmr fragments
1.0 m

magma chamber 1, visc(time), Ra.init-2 x 10^7

temperature at time(yrs) 5.688e-04

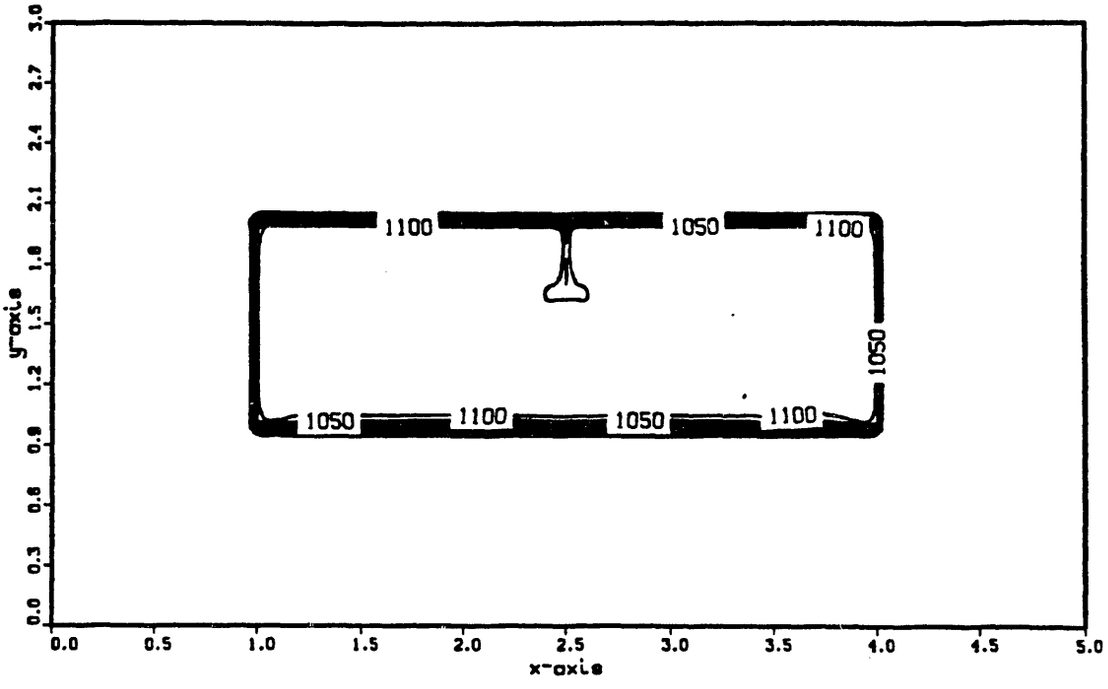

temperature at time(yrs) 2.738e-03

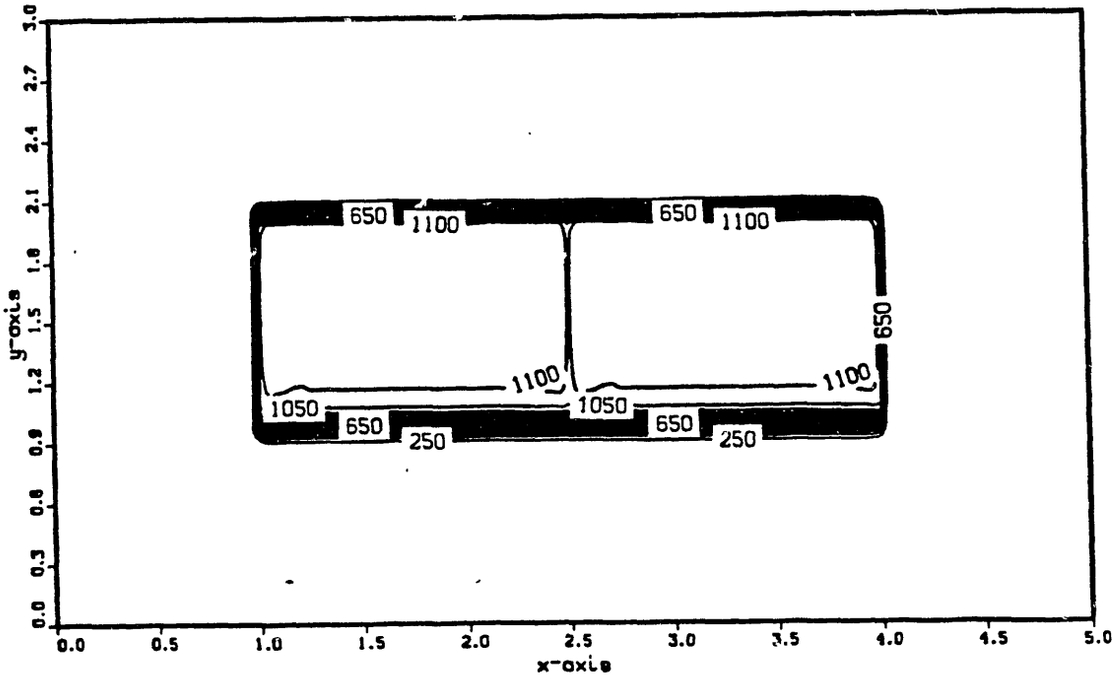

Fig. 6

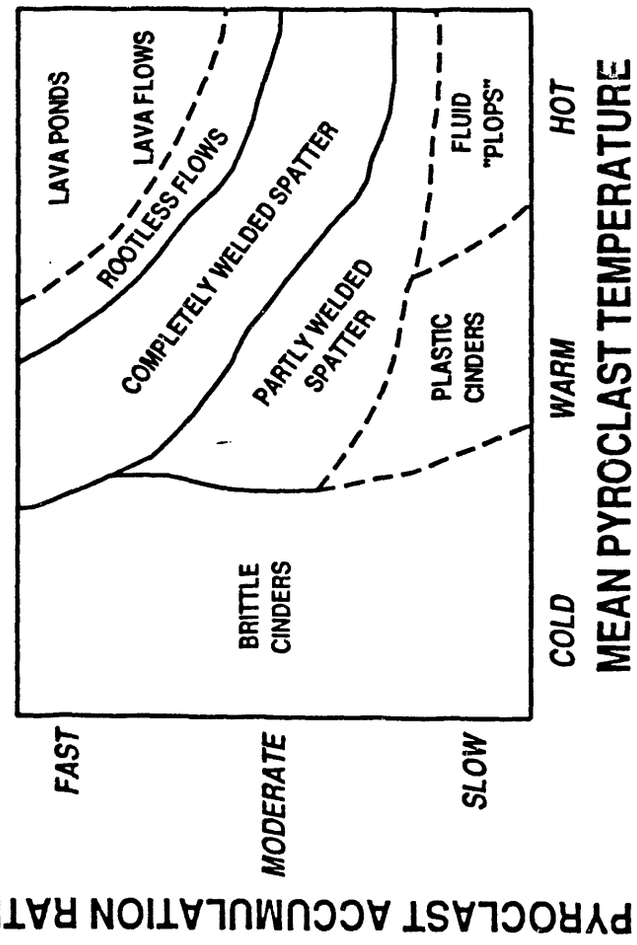
LAVA PONDS
LAVA FLOWS
ROOTLESS FLOWS
COMPLETELY WELDED SPATTER
PARTLY WELDED SPATTER
PLASTIC CINDERS
FLUID "PLOPS"
BRITTLE CINDERS
COLD
WARM
HOT
MEAN PYROCLAST TEMPERATURE
FAST
MODERATE
SLOW
PYROCLAST ACCUMULATION RATE

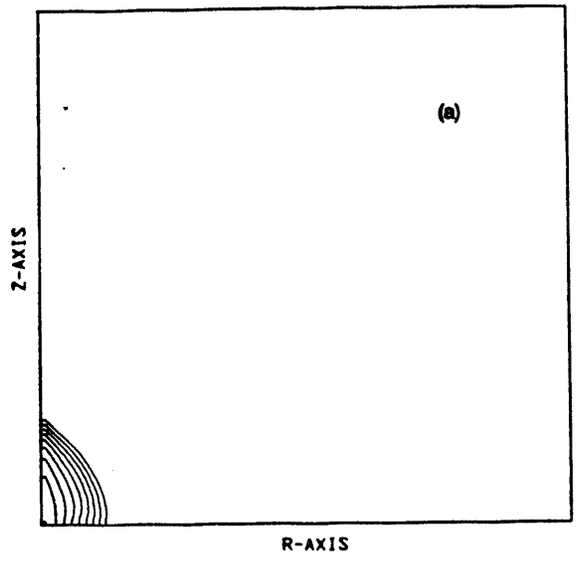
(a)
Z-AXIS
R-AXIS

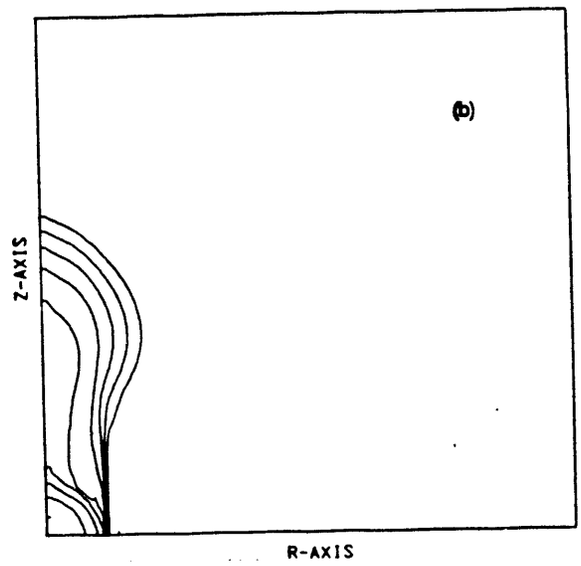
(b)
Z-AXIS
R-AXIS

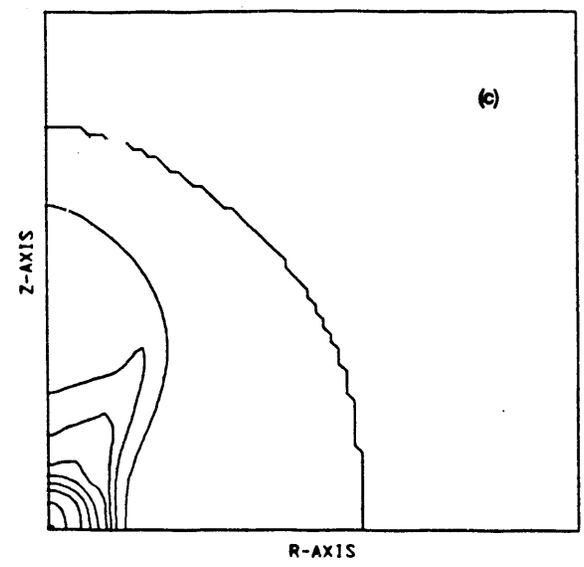
(c)
Z-AXIS
R-AXIS

Figure 8

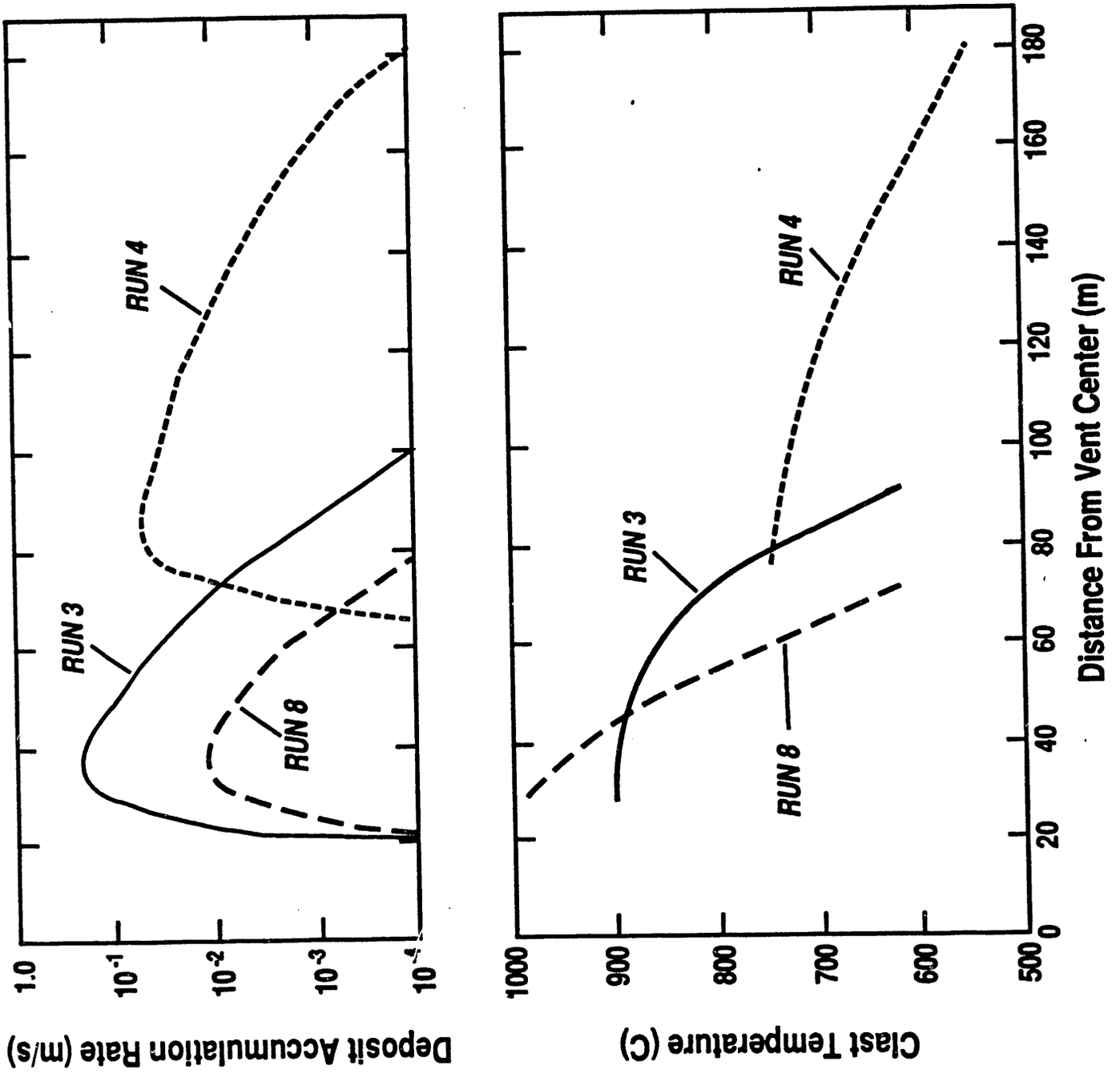
RUN 4
RUN 3
RUN 8
1.0
10^{-1}
10^{-2}
10^{-3}
10^{-4}
Deposit Accumulation Rate (m/s)
RUN 4
RUN 3
RUN 8
1000
900
800
700
600
500
0
20
40
60
80
100
120
140
160
180
Distance From Vent Center (m)
Clast Temperature (C)

Figure 9

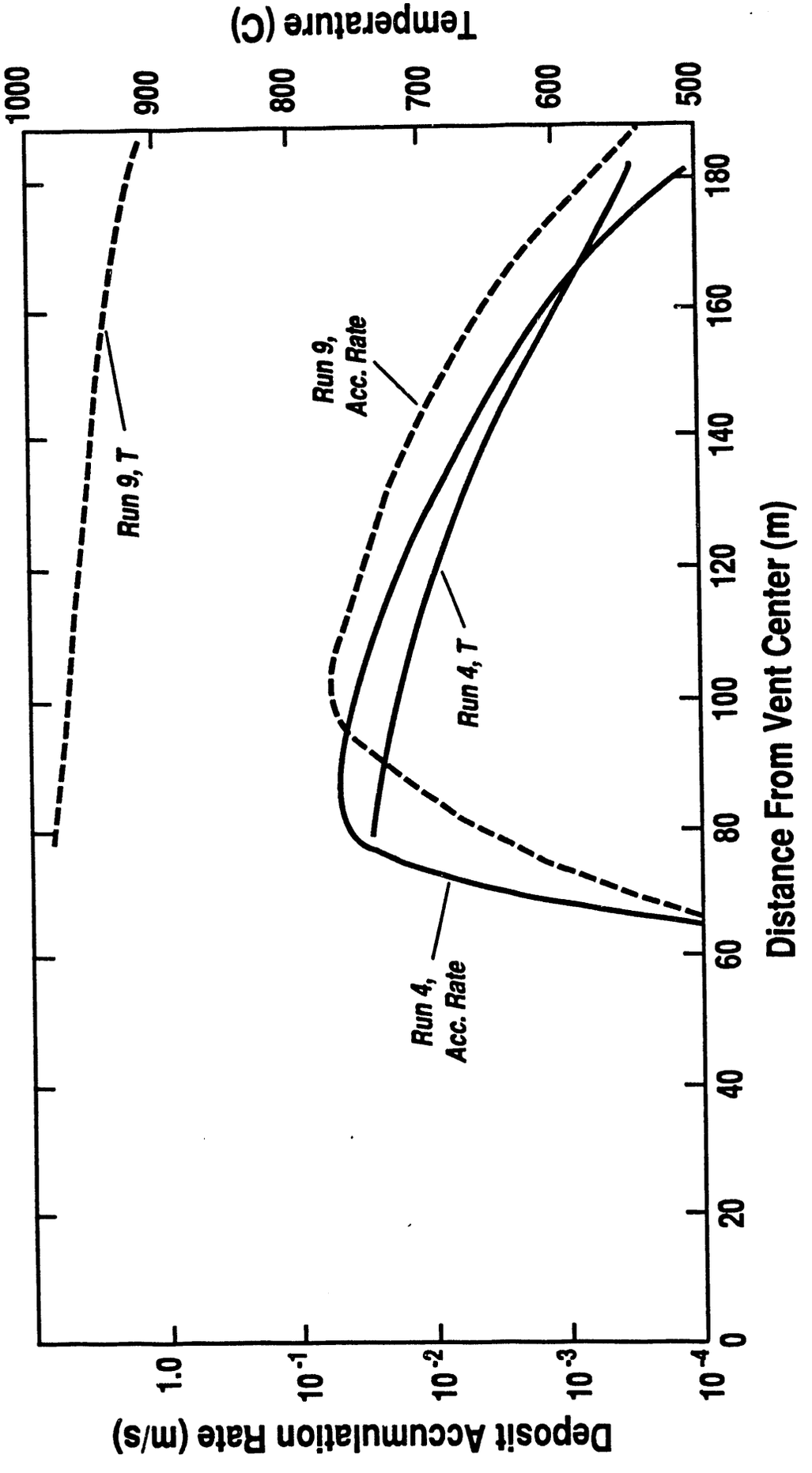
Temperature (C)
1000
900
800
700
600
500
Run 9, T
Run 9, Acc. Rate
Run 4, T
Run 4, Acc. Rate
Deposit Accumulation Rate (m/s)
1.0
10-1
10-2
10-3
10-4
0
20
40
60
80
100
120
140
160
180
Distance From Vent Center (m)

END

DATE
FILMED
3/6/92